IFU spectroscopy of southern planetary nebulae – III

A. Ali,[1,2]★ M. A. Dopita,[1,3]★ H. M. Basurah,[1] M. A. Amer,[1,2] R. Alsulami[1]
and A. Alruhaili[1]

[1]*Astronomy Department, Faculty of Science, King Abdulaziz University, 21589 Jeddah, Saudi Arabia*
[2]*Department of Astronomy, Faculty of Science, Cairo University, 12613 Giza, Egypt*
[3]*Research School of Astronomy and Astrophysics, Australian National University, Cotter Rd., Weston, ACT 2611, Australia*

ABSTRACT

In this paper, we describe integral field spectroscopic observations of four southern Galactic planetary nebulae (PNe), M3-4, M3-6, Hen2-29 and Hen2-37 covering the spectral range 3400–7000 Å. We derive the ionization structure, the physical conditions, the chemical compositions and the kinematical characteristics of these PNe and find good agreement with previous studies that relied upon the long-slit technique in their co-spatial area. From their chemical compositions as well as their spatial and kinematic characteristics, we determined that Hen2-29 is of the Peimbert type I (He- and N-rich), while the other three are of type II. The strength of the nebular He II line reveals that M3-3, Hen2-29 and Hen2-37 are of mid to high excitation classes while M3-6 is a low-excitation PN. A series of emission-line maps extracted from the data cubes were constructed for each PN to describe its overall structure. These show remarkable morphological diversity. Spatially resolved spectroscopy of M3-6 shows that the recombination lines of C II, C III, C IV and N III are of nebular origin, rather than arising from the central star as had been previously proposed. This result increases doubts regarding the weak emission-line star (WELS) classification raised by Basurah et al. In addition, they reinforce the probability that most genuine cases of WELS arise from irradiation effects in close binary central stars.

Key words: ISM: abundances – planetary nebulae: individual: M3-4 – planetary nebulae: individual: M3-6 – planetary nebulae: individual: He2-29 – planetary nebulae: individual: Hen2-37.

1 INTRODUCTION

The vast majority of the spectroscopic studies of PNe up to the present day have relied upon long-slit spectroscopic techniques. However, these measurements sample only a portion of the complete nebula, and are of necessity weighted towards the high-ionization regions around the central star (CS). An accurate determination of the physical and chemical nebular parameters, as well as the determination of their global parameters, requires knowledge of their integrated spectra and spatial structure. The advent of integral field units (IFUs) now provides an opportunity to obtain these data, and to build fully self-consistent photoionization models for PNe. The IFU technique as applied to PNe was pioneered by Monreal-Ibero et al. (2005) and Tsamis et al. (2007). Recently, detailed physical and morpho-kinematical studies using optical IFU data have been taken by Danehkar & Parker (2015) and Danehkar (2015) to study the PNe Hen 3-1333, Hen 2-113 and Th 2-A.

The Wide Field Spectrograph (WiFeS) instrument mounted on the 2.3 m ANU telescope at Siding Spring Observatory (Dopita et al. 2007, 2010) offers the ability to perform such IFU spectroscopy, since it is capable of reaching a spatial resolution of 1.0 arcsec, a spectral coverage of 3200–8950 Å and a spectral resolution of $R = 7000$. Combined with a field of view of 25 arcsec × 38 arcsec, it is very well suited to integral field spectroscopy of compact PNe. The first paper in this series by Ali et al. (2015b) used WiFeS to study the large, evolved and interacting planetary nebula PN G342.0−01.7, generating an IFU mosaic to cover the full spatial extent of the object. In the second, Basurah et al. (2016) provided a detailed analysis of four highly excited non-type I PNe which casts doubt on the general applicability of the weak emission-line star (WELS) classification. Here, and in upcoming studies, we aim to further exploit the capabilities of the WiFeS instrument to provide a new data base on previously studied, bright and compact PNe. Specifically, our objectives are to

(i) create emission-line maps for PN in any diagnostic emission line within its spectral range;

★ E-mail: afmali@kau.edu.sa (AA); Michael.Dopita@anu.edu.au (MAD)

(ii) provide integrated spectra of the whole PN, and if possible, of its exciting star;

(iii) analyse these spectra both in the forbidden and recombination lines to derive chemical abundances and to understand any differences between results obtained here and through long-slit observations of the same objects;

(iv) determine expansion velocities and the kinematic nature of the PN;

(v) build self-consistent photoionization models to derive abundances, physical conditions within the nebula, to determine distances and to place the PNe on the Hertzsprung–Russell diagram in order to derive CS masses, the evolutionary status and the nebular age.

Emission-line mapping of PNe has previously been obtained through the technique of narrow-band interference filter imaging (e.g. Manchado et al. 1996; Górny et al. 1999; Hajian et al. 2007; Miranda, Ramos-Larios & Guerrero 2010; Aller et al. 2015; García-Rojas et al. 2016). The difficulty here is that each image is very expensive in observing time, and only one emission line can be imaged at once. On the other hand, IFU spectroscopy makes available the narrow-band images of all lines which are observed with sufficient signal-to-noise ratio. Emission-line maps and line ratio maps provide us structural details and physical processes. For example,[O III]/Hα ratio maps are useful to study the variation of ionization and chemical abundances and also to look for signatures of collimated outflows and shocks (Guerrero et al. 2013), [S II]/Hα ratio maps are particularly sensitive to shocked regions (Akras & Gonçalves 2016; Akras et al. 2016), whereas He II/Hα ratio maps identify the very high ionization regions (Vázquez 2012).

The main objective of the current paper is to study four Galactic PNe – M3-4, M3-6, He2-29 and Hen2-37 – which have so far received relatively little attention. In this paper, we will use WiFeS data to examine the correlations between nebular morphology and excitation. Furthermore, the WiFeS instrument is ideally suited to study spatial variations in nebular parameters, such as extinction, electron temperature, density and ionic abundances.

Górny et al. (1999) imaged Hen2-29 and Hen2-37 in a narrowband Hα filter and determined angular sizes of 20 arcsec ×16 arcsec and 27 arcsec × 24 arcsec, respectively. Corradi, Aznar & Mampaso (1998) classified Hen2-29 and Hen2-37 nebulae as elliptical PNe with modest ellipticity (major-to-minor axis length ratio ≤ 1.3) and outer irregular contours. Searching the literature and the ESO archive, it would appear that no narrow-band images are available for M3-4 and M3-6. However, spectroscopic studies of all four PNe are to be found distributed across several papers, e.g. Milingo, Henry & Kwitter (2002), Martins & Viegas (2000), Maciel & Quireza (1999), Kingsburgh & Barlow (1994), Chiappini & Maciel (1994) and Perinotto, Morbidelli & Scatarzi (2004).

In this paper, we present excitation maps, integral field spectroscopy and an abundance analysis of these four PNe. The observations and data reduction are described in Section 2, while the emission-line maps are presented and discussed in Section 3. In Section 4, we use the spectrophotometry to derive the physical conditions, ionic and elemental abundances, and excitation class (EC) determinations. Section 5 gives kinematical signatures such as the expansion and radial velocities and the distances. In Section 6, we provide a discussion of the classification of the CS in M3-6, and our conclusions are given in Section 7.

2 OBSERVATIONS AND DATA REDUCTION

The integral field spectra of the PNe were obtained over two nights of 2013 March 31 and April 01 with the WiFeS instrument. This instrument delivers a field of view of 25 arcsec × 38 arcsec at a spatial resolution of either 1.0 arcsec × 0.5 arcsec or 1.0 arcsec × 1.0 arcsec, depending on the binning on the CCD. The design of the image slicer means that there is essentially no clear space between pixels – the spatial filling is ∼98 per cent. In these observations, we operated in the binned 1.0 arcsec × 1.0 arcsec mode. The data cover the blue spectral range of 3400–5700 Å at a spectral resolution of $R \sim 3000$ that corresponds to a full width at half-maximum (FWHM) of ∼100 km s^{-1} (∼1.5 Å), while in the red spectral range of 5500–7000 Å we used the higher spectral resolution grating $R \sim 7000$ corresponding to an FWHM of ∼45 km s^{-1} (∼0.9 Å).

The wavelength scale was calibrated using the Cu-Ar arc lamp with 40 s exposures throughout the night, while flux calibration was performed using the STIS spectrophotometric standard stars HD 111980 and HD 031128.[1] In addition, a B-type telluric standard HIP 38858 was observed. Telluric absorption features from atmospheric oxygen (O$_2$) and water (H$_2$O) are corrected with PYWIFES[2] data reduction pipeline (Childress et al. 2014) as follows. First, the absorption for each telluric standard is measured by fitting a smooth low-order polynomial (typically a cubic function) to the stellar continuum redwards of 6000 Å, and dividing the observed spectrum by this smooth continuum fit. Then, the effective mean absorption at zenith for each component (O$_2$ and H$_2$O) is computed for each observed telluric standard by scaling the observed absorption to airmass 1 using the appropriate scaling of optical depth with airmass for each component. We note that the O$_2$ bands are typically saturated, while the H$_2$O bands are not, so they have different airmass dependences. In addition, the relative humidity in the various atmospheric layers ensures that the H$_2$O absorption components vary relative to the O$_2$ absorption. The mean zenith absorption profiles for the two components (O$_2$ and H$_2$O) can then be similarly scaled to the airmass of any observed science field, and the WiFeS data cube is divided by the expected telluric absorption profile. A similar technique can be employed with single telluric standards whose absorption profiles are used to correct an individual science data cube.

All data cubes were reduced using the PYWIFES. A summary of the spectroscopic observations is given in Table 1. In some objects, due to the saturation of strong nebular emission lines such as [O III] λ5007 and Hα, the fluxes in these lines were derived from additional frames with short exposure times.

The global spectra of each of the objects were extracted from their respective data cubes using a circular aperture matching the observed extent of the bright region of the PNe using QFitsView v3.1 rev.741.[3] The line fluxes measured in blue and red spectra were slightly re-scaled (by a factor of ∼2 per cent) using the emission lines in the overlapping spectral range (5500–5700 Å). This procedure allows for sub-arcsec differences in the extraction apertures caused by differential atmospheric dispersion.

Emission-line fluxes and their uncertainties were measured, from the final combined, flux-calibrated blue and red spectra, using the

---

[1] Available at www.mso.anu.edu.au/~bessell/FTP/Bohlin2013/GO12813.html

[2] http://www.mso.anu.edu.au/pywifes/doku.php.

[3] QFitsView v3.1 is a FITS file viewer using the QT widget library and was developed at the Max Planck Institute for Extraterrestrial Physics by Thomas Ott.

Table 1. The observing log.

Nebula name	PNG number	No. of frames	PA (deg)	Exposure time (s)	Date	Airmass	Standard star
M3-4	PN G241.0+02.3	3	90	600	31/3/2013	1.01	HD 111980 and HD 031128
M3-6	PN G253.9+05.7	6	0	300	31/3/2013	1.01	HD 111980 and HD 031128
		3	0	50	31/3/2013	1.00	HD 111980 and HD 031128
Hen2-29	PN G275.8−02.9	3	45	600	01/4/2013	1.23	HD 111980 and HD 031128
		1	45	300	01/4/2013	1.23	HD 111980 and HD 031128
Hen2-37	PN G274.6+03.5	3	90	600	31/3/2013	1.06	HD 111980 and HD 031128
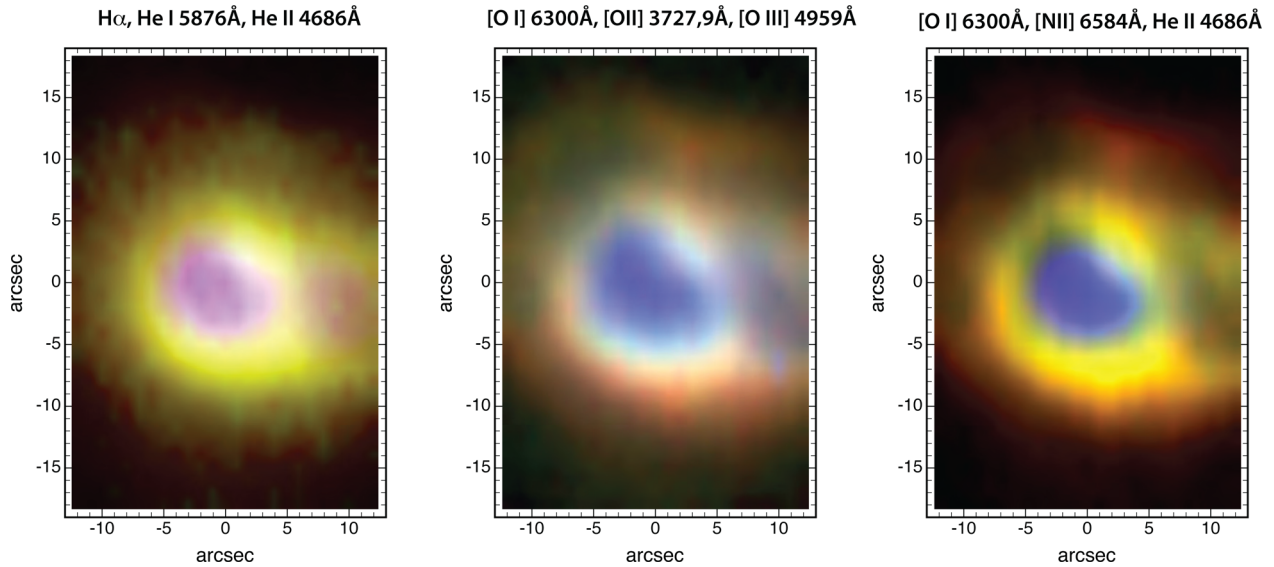
Figure 1. A series of narrow-band emission-line maps for M3-4. In this figure, east is at the top of the image, and north is to the right. The colour channels (R, G and B, respectively) used for the emission-line images are given above each panel. The first panel (Hα, He I λ5876 and He II λ4686) gives the clearest idea of the flux distribution in the nebula since all three are recombination lines. The high-ionization regions appear purple and occupy roughly the central part of the nebula, while the lower ionization regions appear yellow and surround the high-ionization regions. The remaining two panels are designed to bring out the ionization stratification of the nebula in the oxygen ions (central panel) and in [O I] λ6300, [N II] λ6584 and He II λ4686 respectively (right-hand panel). This nebula has a complex double-shell and bipolar structure.

IRAF `splot` task.[4] Each line was fitted with multi-Gaussians, as necessary.

3 NEBULAR MORPHOLOGY

Emission-line maps of the brightest lines were constructed using the reduced WiFeS data cubes for each nebula in our set. These maps are used to describe their internal flux distributions and their excitation structure, by combining three lines into an RGB image. We have selected three such images for inclusion here, and these are presented for each nebula in Figs 1–4.

First, a combination of Hα, He I λ5876 and He II λ4686 (left-hand panels in Figs 1–4) provides the emissivity distribution in the principal recombination lines. Since Hα is distributed throughout the nebula, in regions where helium is not ionized, these maps will be dominated by the Hα flux, and will appear red. In regions where helium is singly ionized, the map will appear yellow (R+G), while

in regions in which the He II λ4686 line is seen, the map will appear mauve (R+B).

The second combination of the lines [O I] λ6300, [O II] λ3727, 9 and [O III] λ5007 – the central panels in Figs 1–4 – brings out the ionization stratification very clearly. Finally, as a different way of bringing out the ionization structure, we give the [O I] λ6300, [N II] λ6584 and He II λ4686 image (right-hand panels in Figs 1–4). This combination covers a more extreme range in ionization potential than the central panels.

These four PNe have very different morphologies. M3-4 (Fig. 1) has a very complex bipolar double-shell structure with two lobes in which He II λ4686 is strong. The appearance of the inner bright rings suggests that they represent an incomplete bipolar shell. The ionization stratification across these rings is clearly evident. This double-ring structure is embedded in an outer shell dominated by the [O I] λ6300 emission. The outer shell has similar morphology to the inner, but it extends beyond the field of view of this WiFeS frame. The green tones in the upper-left and upper-right quadrants of the central panel show that the outer shell is of intermediate excitation with strong [O II] λ3727, 9 emission.

M3-6 (Fig. 2) appears as an elliptical PN with brightness increasing towards the centre. Overall, the nebula is of lower excitation than M3-4, and the He II λ4686 emission has its origin in the CS.

---

[4] IRAF is distributed by the National Optical Astronomy Observatory, which is operated by the Association of Universities for Research in Astronomy (AURA) under a cooperative agreement with the National Science Foundation.
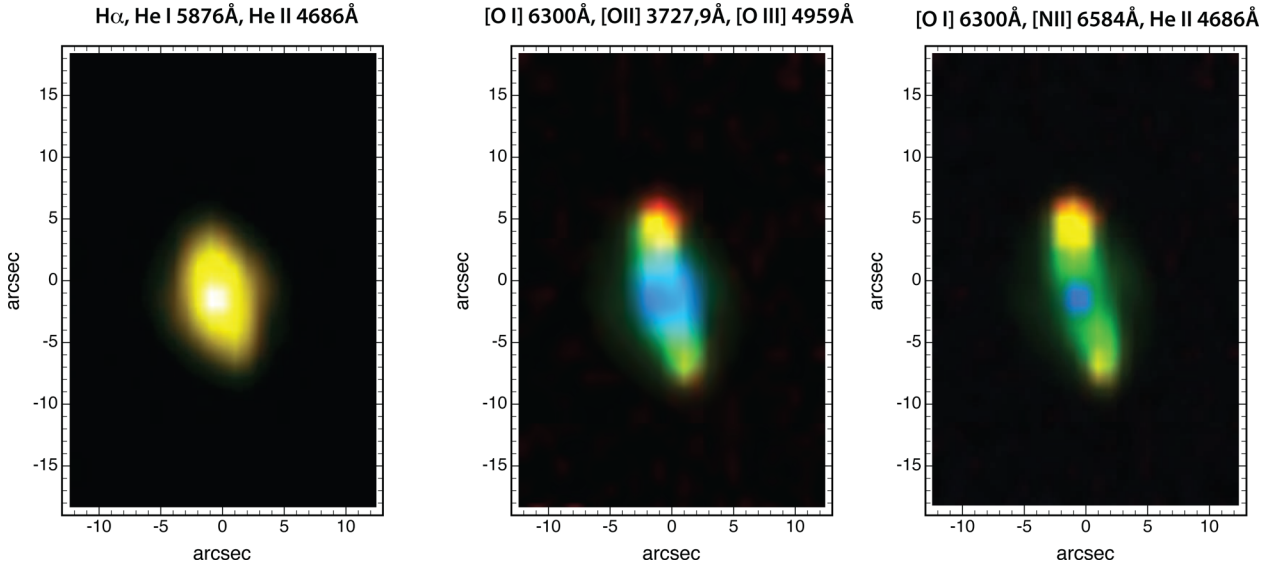
Figure 2. As Fig. 1, but for M3-6. In this figure, north is at the top of the image, and east is to the left. This object has a bright CS (visible here in its He II λ4686 emission) with a strongly elliptical morphology with 'ansae'. In the excitation maps, these ansae are visible in the low-ionization species [O I], [N II] and [O II]. The outermost knots of emission in [O I] are probably identified as fast low-excitation emission-line regions (FLIERs). For more discussion, see the text.
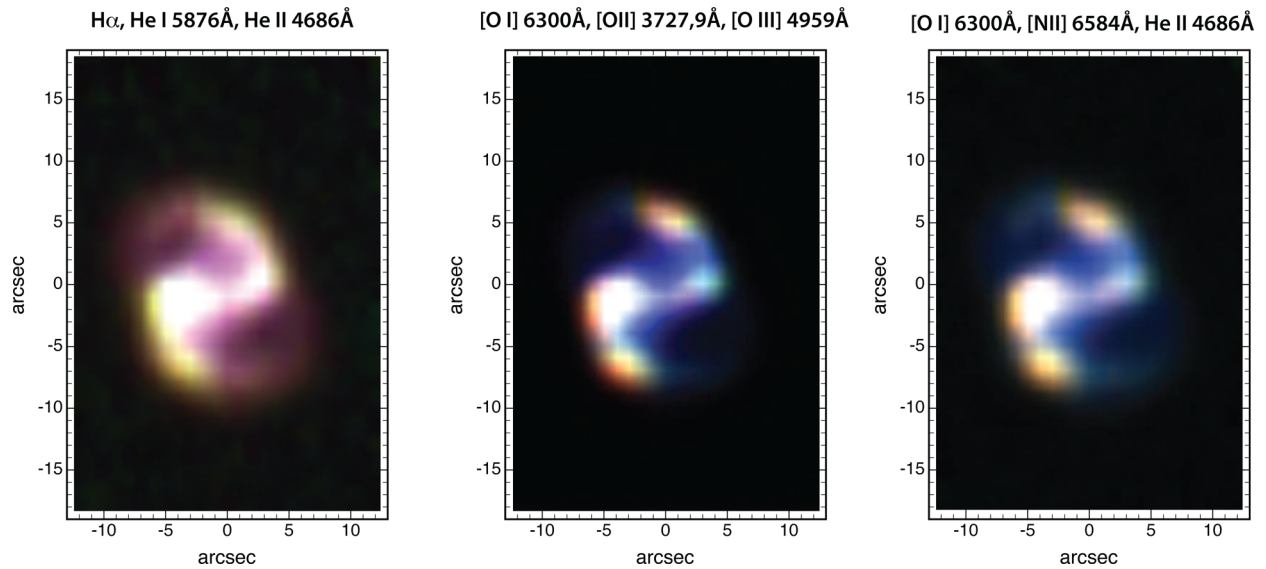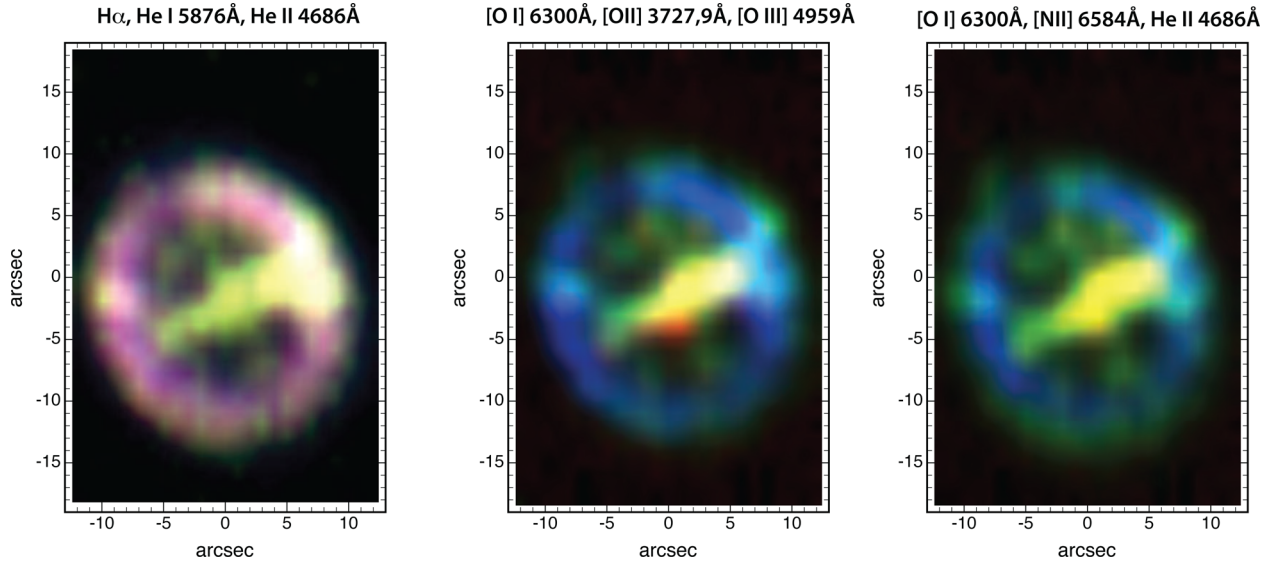

Figure 3. As Fig. 1, but for Hen2-29. In this figure, NE is at the top of the image, and SE is to the left. This nebula is highly bisymmetric with four low-excitation regions embedded in a two-arm barred spiral structure.

It shows pronounced 'ansae' along PA∼20 deg. At the ends of these ansae are two bright knots very prominent in [O I] λ6300 and [S II] λ6717, 31. These are almost certainly fast low-excitation emission-line regions (FLIERs; Balick, Preston & Icke 1987; Balick et al. 1993, 1994). These regions are almost certainly shock-excited by a convergent fast stellar wind flow shaped by the density and/or magnetic structure of the earlier asymptotic giant branch (AGB) wind (Dopita 1997; Steffen, López & Lim 2002). However, the radial velocities of these two knots are very little different – we measure the northern knot to have a heliocentric radial velocity of 34.7 ± 3.4 km s^{-1} and the southern one at 23.8 ± 3.3 km s^{-1}. If our hypothesis on their origin is correct, the knots must lie almost in the plane of the sky. In Table 7, we determine an overall heliocentric velocity of 31.1 ± 3.5 for the nebula which supports our interpretation.

At very low flux levels, we also detected a faint extended halo surrounding the bright nebula and extending over a region of ∼14 arcsec × 20 arcsec. This may be the ionized trace of the earlier AGB wind.

Hen2-29 (Fig. 3) reveals 'a reverse S-shape' or two-arm spiral structure formed by two point-symmetric arcs present along the minor axis within an overall elliptical morphology. The densest regions in the arms are also optically thick, while the overall elliptical outline is filled with high-excitation gas.

Finally, Hen2-37 (Fig. 4) displays a Θ-like morphology overall. The bar of the Θ contains optically thick material, and there are isolated lower recitation knots embedded in the body of the nebula in a region of otherwise low density. The high-excitation regions are confined to a region within the outer circle of the Θ, and is

Figure 4. As Fig. 1, but for Hen2-37. In this figure, east is at the top of the image, and north is to the right. The Θ-like morphology of this nebula probably arises by interaction of a symmetric fast wind with a dense equatorial disc of material ejected during the AGB phase of evolution. This region also contains a number of denser knots undergoing photoevaporation.

bounded at its outer boundary by lower excitation gas. Here, we might interpret the bar of the Θ as a remnant of a dense equatorial ring of martial ejected during the AGB phase, the knots as being photoevaporating inclusions embedded in the fast stellar wind region, and the outer ring as being the swept-up shell of denser AGB wind gas.

4 DETERMINATION OF PHYSICAL CONDITIONS AND ABUNDANCES

4.1 Line intensities and reddening corrections

The global emission-line spectra are summarized in Table 2. These have been analysed using the Nebular Empirical Abundance Tool (NEAT;[5] Wesson, Stock & Scicluna 2012). The code was applied to derive the interstellar extinction coefficient and subsequent nebular parameters such as temperature, density and ionic and elemental abundances. The line intensities have been corrected for extinction by adopting the extinction law of Howarth (1983), where the amount of interstellar extinction was determined from the ratios of hydrogen Balmer lines, in an iterative method. First, an initial value for the extinction coefficient, $c(H\beta)$, was calculated by the code. This value was derived from the intrinsic $H\alpha$, $H\beta$, $H\gamma$ line ratios, assuming an electron temperature (T_e) of 10 000 K and electron density (N_e) of 1000 cm^{-3}. Secondly, the code calculates the electron temperature and density as explained in the coming section. Thirdly, the intrinsic Balmer line ratios were re-calculated at the appropriate temperature and density, and again $c(H\beta)$ was re-calculated. No spatial reddening variation was detected throughout any of the PN set, except in the case of M3-6. The two low-ionization condensations which lie along its major axis show a lower extinction compared to the main nebula.

Table 3 lists the estimated reddening coefficients and the observed $H\beta$ and $H\alpha$ fluxes on a log scale. The complete list of the

[5] The code, documentation and atomic data are freely available at http://www.nebulousresearch.org/codes/neat/.

observed and de-reddened line strengths is given in Table 2. Here, columns 1 and 2 give the laboratory wavelengths (λ_{Lab}) and the line identifications of observed emission lines, respectively. Columns 3–14 give the observed wavelength (λ_{Obs}), fluxes $F(\lambda)$ and fluxes corrected for reddening $I(\lambda)$ relative to $H\beta = 100$. The Monte Carlo technique was used by NEAT to propagate the statistical uncertainties from the line flux measurements through to the derived abundances. Both line ratios [O III] $\lambda5007/\lambda4959$ and [N II] $\lambda6584/\lambda6548$ were measured to be in the range of (2.9–3.1) which are comparable to the theoretical predictions of 2.98 (Storey & Zeippen 2000) and 2.94 (Mendoza 1983), respectively.

4.2 Optical thickness estimates

The low-ionization [N I] doublet $\lambda\lambda5197, 5201$ is present in the spectra of M3-4, Hen2-29 and Hen2-37. It is known that this line and other low-ionization species such as [O I] $\lambda6300, 6363$ arise in the outermost part of the nebula. Due to the charge-transfer reaction rate, it is expected that both [O I] and [N I] are abundant in the warm transition region between the neutral and ionized nebular envelopes (Liu et al. 1995). If shocks are present, the intensity of these lines is increased thanks to the increase in collision strength with electron temperature. In the case of M3-4 nebula, both [N I] and [O I] are present in the external parts of the object. By contrast, in Hen2-37 we found traces of [N I] and [O I] in the central region of the object (see Fig. 4, central panel), showing that the bar of the Θ is composed of material which is optically thick to the radiation field. In the case of Hen2-29, the [N I] gas appears distributed in several regions of high emissivity (see Fig. 3). Using [N I] line ratio $\lambda5197/\lambda5201$, we estimate ionic densities of 378 and 412 cm^{-3} for M3-4 and Hen2-29, respectively. These estimates are in good agreement with the other nebular density measurements listed in Table 4.

In the case of Hen2-37, we can crudely estimate an electron temperature, $T_e = 14\,700$ K, from the [O I] $\lambda\lambda5577/6300$ line ratio for Hen2-37 nebula. This value is higher than the temperatures derived from [O III] and [N II] lines (Table 4), and may indicate the presence of a shock contribution.

Table 2. Integrated line fluxes and the derived de-reddened line intensities for M3-4, M3-6, Hen2-29 and Hen2-37. Absolute line fluxes for Hβ are given in the text. The C IV doublet lines 5801+5812 Å are of CS origin. The full version of the table is available online. A portion is shown here for guiding the reader regarding its content.

λ_{Lab} (Å)	ID	M3-4			M3-6			Hen2-29			Hen2-37		
		λ_{Obs} (Å)	$F(\lambda)$	$I(\lambda)$	λ_{Obs} (Å)	$F(\lambda)$	$I(\lambda)$	λ_{Obs} (Å)	$F(\lambda)$	$I(\lambda)$	λ_{Obs} (Å)	$F(\lambda)$	$I(\lambda)$
4685.68	He II	4686.29	33.2 ± 0.99	34.0 ± 1.51	4686.47	0.2 ± 0.02	0.2 ± 0.02	4685.20	65.6 ± 3.28	71.7 ± 5.35	4685.20	67.9 ± 3.40	73.3 ± 5.48
4711.37	[Ar IV]	4712.13	2.2 ± 0.34	2.3 ± 0.36	4711.56	0.3 ± 0.11	$0.3^{+0.06}_{-0.08}$	4710.86	3.7 ± 0.39	4.0 ± 0.48	4710.80	3.4 ± 0.32	3.6 ± 0.40
4714.17	[Ne IV]							4713.34	0.8 ± 0.17	$0.7^{+0.132}_{-0.163}$	4713.55	0.3 ± 0.06	$0.3^{+0.054}_{-0.066}$
4724.89	[Ne IV]b							4724.20	0.8 ± 0.12	0.9 ± 0.14	4724.20	0.6 ± 0.09	0.6 ± 0.10
4740.17	[Ar IV]	4740.76	1.7 ± 0.25	1.7 ± 0.26	4740.52	0.4 ± 0.05	0.4 ± 0.06	4739.70	2.9 ± 0.29	3.1 ± 0.35	4739.50	2.3 ± 0.23	2.5 ± 0.28
4861.33	H I 4-2	4861.79	100.0 ± 3.00	100.0 ± 0.00	4861.55	100.0 ± 5.00	100.0 ± 0.00	4860.70	100.0 ± 5.00	100.0 ± 0.00	4860.60	100.0 ± 0.00	100.0 ± 0.00
4921.93	He I	4922.8	0.9 ± 0.14	0.9 ± 0.14	4922.11	1.2 ± 0.19	1.2 ± 0.20	4921.30	1.2 ± 0.12	1.2 ± 0.13	4921.20	0.9 ± 0.13	0.9 ± 0.14
4958.91	[O III]	4959.38	403.3 ± 12.10	398.2 ± 16.63	4959.11	232.2 ± 11.61	227.3 ± 15.95	4958.30	566.6 ± 28.3	540.8 ± 37.42	4958.20	722.8 ± 36.14	695.5 ± 48.36
5006.84	[O III]	5007.28	1198.9 ± 36.0	1175.6 ± 48.9	5007.02	695.4 ± 34.8	673.1 ± 47.0	5006.20	1696.3 ± 84.8	1582.4 ± 107.3	5006.20	2238.3 ± 111.9	2110.7 ± 145.2

The strength of [O II] and [N II] emission lines was used by Kaler & Jacoby (1989) to help define the optical thickness of PNe. Following their criteria, we verified that Hen2-37 nebula is probably optically thick to the ionizing radiation field (radiation bounded). It displays strong low-excitation lines, with $F([N\,II]\,\lambda6583) \geq F(H\alpha)$ and $F([O\,II]\,\lambda3727)/F(H\beta) \geq 1.5$. By contrast, the nebula M3-6 is optically thin (density bounded), except within the ansae. This is supported by several lines of evidence: (1) the weakness of the low-excitation lines [O I], [O II] and [N II]; (2) a line ratio $F([N\,II]\lambda6583)/F(H\alpha) \leq 0.1$; (3) the absence of detectable [N I] at $\lambda5200$. The other two nebulae in the sample appear partially optically thick PNe. M3-4 and Hen2-29 have $F[N\,II](\lambda6583)/F(H\alpha)$ = 0.9, $F[O\,II](\lambda3727)/F(H\beta) = 1.25$, $F[N\,II](\lambda6583)/F(H\alpha) = 0.75$ and $F[O\,II](\lambda3727)/F(H\beta) = 1.56$, respectively.

4.3 Temperatures and densities

The observed emission lines in our sample (Table 2) permitted us to estimate the electron temperature and density from both the low- and the medium-ionization zones. The low-ionization species provide the nebular temperature from the [N II] $(\lambda6548 + \lambda6584)/\lambda5754$ line ratio and the density from the [S II] $\lambda6716/\lambda6731$ and the [O II] $\lambda3727/\lambda3729$ line ratios. The moderately excited species provide the nebular temperature from the [O III] $(\lambda4959 + \lambda5007)/\lambda4363$ line ratio and the density from the [Cl III] $\lambda5517/\lambda5537$ and [Ar IV] $\lambda4711/\lambda4740$ line ratios. The temperatures derived from [O III] lines are consistently higher than those derived from the [N II] lines, except in the case of the optically thin object M3-6.

In Table 4, we list the calculated nebular temperatures, densities and their uncertainties for each object. In addition, it also provides comparisons of our results with those which have previously appeared in the literature. In almost cases, we find good agreement with other works. As expected, temperatures derived from [O III] lines are consistently higher than those derived from the [N II] lines, except in the case of the optically thin object M3-6.

4.4 Ionic and elemental abundances

Applying the NEAT, ionic abundances of nitrogen, oxygen, neon, argon, chlorine and sulphur were calculated from the collisionally excited lines (CEL), while helium and carbon were calculated from the optical recombination lines using the temperature and density appropriate to their ionization potential. When several lines from a given ion are present, the adopted ionic abundance was taken averaging the abundances from each line weighted according to their line intensities. The total elemental abundances were calculated from ionic abundances using the ionization correction factors (ICF) given by Kingsburgh & Barlow (1994) to correct for unseen ions. The helium elemental abundances for all objects were determined from the He^+/H and He^{2+}/H ions, assuming ICF (He) = 1.0. The carbon elemental abundances were determined from C^{2+}/H for all objects, except in the case of Hen2-29 where we used both C^{2+}/H and C^{3+}/H taking ICF (C) = 1.0. In general, the chemical abundances are found to be in good agreement with other works which are presented in Tables 5 and 6.

4.5 EC and Peimbert classification

Our objects (Table 2) display a mixture of both low- and high-excitation emission lines. Furthermore, the highly ionized species [Ne V] appears in M3-4, Hen2-29 and Hen2-37. The line strength of He II $\lambda4686$ Å relative to Hβ provides a best quantitative measure

Table 3. Reddening coefficients and observed Hβ and Hα fluxes of PNe set.

Object	c(Hβ)		Log F(Hβ)		Log F(Hα)	
	This work	Other works	This work	Other works	This work	Other works
M3-4	0.25	0.2[a], 0.38[b], 0.70[c], 0.23[d]	−12.43	−12.4[g], −12.60[b]	−11.49	−11.46[i]
M3-6	0.43	0.64[a], 0.35[b], 0.58[c], 0.49[e], 0.53[f]	−11.01	−11.1[g], −11.22[b], −12.0[e]	−10.41	−10.36[i]
Hen2-29	0.87	1.01[a], 0.63[c]	−12.17	−12.1[g], −12.17[h]	−11.44	−11.40[i]
Hen2-37	0.74	0.80[a], 0.69[b], 1.03[c]	−12.28	−12.4[g], −12.73[b], −12.40[h]	−11.60	−11.53[i]

References. [a]Tylenda et al. (1992); [b]Milingo et al. (2002); [c]Kingsburgh & Barlow (1994); [d]Kniazev (2012); [e]Girard, Köppen & Acker (2007); [f]De Freitas Pacheco, Maciel & Costa (1992); [g]Acker et al. (1991); [h]Perinotto et al. (2004); [i]Frew, Bojičić & Parker (2013).

Table 4. Electron temperatures and densities of the PNe set.

Object	Temperature (K)				Density (cm^{-3})			
	[O III]	[N II]	[S II]	[Ar V]	[S II]	[O II]	[Ar IV]	[Cl III]
M3-4	$11\,154^{+396}_{-396}$	$10\,267^{+227}_{-227}$			362^{+132}_{-229}	721^{+185}_{-147}	285^{+166}_{-220}	1202^{+720}_{-516}
Ref (1)	11 500	9300	8500		200			
Ref (2)	$12\,100^{+1000}_{-1000}$	9900			100^{+}			
Ref (3)	$12\,103^{+360}_{-360}$				322^{+142}_{-142}			
M3-6	7988^{+212}_{-212}	$10\,156^{+485}_{-485}$			2568^{+685}_{-541}	4289^{+1768}_{-4289}	2196^{+725}_{-593}	2013^{+443}_{-605}
Ref (1)	8000	8700			1700			
Ref (2)	8800:					3020^{+370}_{-330}		
Ref (4)	8100	11 300			5210			
Ref (5)	9000							
Hen2-29	$14\,329^{+420}_{-420}$	$12\,520^{+272}_{-272}$	$12\,038^{+1542}_{-12\,038}$		855^{+137}_{-137}	1075^{+373}_{-277}	351^{+158}_{-88}	423^{+169}_{-166}
Ref (2)	$17\,100^{+500}_{-600}$	$11\,000^{+3500}_{-2500}$			720^{+300}_{-240}			
Hen2-37	$12\,147^{+300}_{-300}$	$11\,324^{+397}_{-397}$	$10\,743^{+1231}_{-1104}$		361^{+93}_{-93}	697^{+325}_{-193}	209^{+125}_{-83}	341^{+123}_{-188}
Ref (1)	12 000	10 000	10 300		200			
Ref (2)	$12\,600^{+400}_{-200}$	$10\,100^{+200}_{-500}$			190^{+30}_{-30}		1600^{+280}_{-240}	
Ref (6)	12 824	10 169			270			

References: (1) Milingo et al. (2002); (2) Kingsburgh & Barlow (1994); (3) Kniazev (2012); (4) Girard et al. (2007); (5) De Freitas Pacheco et al. (1992); (6) Martins & Viegas (2000). The symbol (+) indicates that the diagnostic ratio is at low density limit, (:) indicates ~50 per cent uncertainty in the measured flux.

of the nebular EC. The absence of the He II line from the nebular spectrum restricts the PNe to be of low excitation class (EC < 5), and where it appears (EC ≥ 5), its strength relative to Hβ can be used to define the EC. To derive the EC of our PN set, we followed the methodology of Meatheringham & Dopita (1991) and Reid & Parker (2010). Both methods use the same scheme to derive the EC of low-excitation PNe, and therefore give the same result. For PNe of EC ≥ 5, Reid & Parker (2010) have upgraded the scheme of Meatheringham & Dopita (1991) by considering also the increase of [O III]/Hβ line ratio with nebular excitation. This line ratio was fixed in the scheme of Meatheringham & Dopita (1991), since in their optically thick models this line ratio 'saturates'. However, many PNe are optically thin, and in this case, the [O III]/Hβ line ratio initially increases with decreasing optical thickness, before finally decreasing for high-excitation objects when the nebula becomes too optically thin. Our results (Table 6) reveal that M3-6 is of low EC, while other three objects are of medium to high EC.

Hen2-29 is the only PN in our set which shows excess in He and N abundances. Thus, it can be classified as a Peimbert type I by applying the two criteria, He/H ≥ 0.125 and N/O ≥ 0.5, as proposed by Maciel & Quireza (1999). These criteria are much rigid than the original criteria, He/H ≥ 0.125 or N/O ≥ 0.5, suggested by Peimbert & Torres-Peimbert (1983). Based on the analysis of

68 PNe, Kingsburgh & Barlow (1994) found that the average helium abundance of type I PNe is increased by a small amount (a factor of 1.2) over non-type I objects. Therefore, they distinguish between type I and non-type I according to the N/O ratio only. They defined type I PNe as those PNe with N/O ≥ 0.8. Following this criterion, we classify all four PNe in our sample as non-type I objects.

The type I PNe were believed to have evolved from the most massive progenitor stars with initial main-sequence mass range 2.4–8.0 M$_\odot$ (Quireza, Rocha-Pinto & Maciel 2007) and consequently they should be associated with the thin Galactic disc and have low velocity dispersion. They also show a wide range of ionization structures. Using the adopted distance and measured radial velocity, we derived a vertical Galactic height $z = 210$ pc and a peculiar velocity[6] $V_P = 19.4$ km s^{-1} for Hen2-29. Previous measurements of the spatial ($z < 300$ pc; Gilmore & Reid 1983) and kinematic characteristics ($V_P < 60$ km s^{-1}; Maciel & Dutra 1992) of this PN show that it belongs to the thin Galactic disc population.

---

[6] The difference between the observed radial velocity corrected for local standard of rest and the velocity determined from the Galactic rotation curve.

Table 5. Abundances derived from the NEAT for M3-4 and M3-6 compared with other works. Neat (1) and Neat (2) refer to the derived abundances using the ICF of Kingsburgh & Barlow (1994) and Delgado-Inglada, Morisset & Stasińska (2014), respectively.

Element	M3-4 Neat (1)	Neat (2)	Ref 1	Ref 2	Ref 3	Ref 4	M3-6 Neat (1)	Neat (2)	Ref 1	Ref 2	Ref 3	Ref 4
He/H	$1.15E-1^{+5.3E-3}_{-5.3E-3}$	$1.15E-1^{+4.3E-3}_{-4.3E-3}$	1.5E−1	1.23E−1	–	–	$1.11E-1^{+5.1E-3}_{-5.1E-3}$	$1.11E-1^{+3.7E-3}_{-3.7E-3}$	1.20E−1	0.90E−1	–	–
C/H	$6.08E-4^{+9.4E-5}_{-9.4E-5}$	$5.86E-4^{+1.4E-4}_{-8.1E-5}$	–	–	–	–	$3.68E-5^{+5.5E-5}_{-5.5E-5}$	$7.80E-4^{+5.5E-5}_{-5.5E-5}$	–	–	–	–
N/H	$2.10E-4^{+3.3E-5}_{-2.2E-5}$	$2.10E-4^{+3.3E-5}_{-2.9E-5}$	1.93E−4	1.6E−4	–	1.74E−4	$6.83E-5^{+3.1E-5}_{-1.3E-5}$	$1.37E-5^{+3.1E-5}_{-3.5E-5}$	0.58E−4	0.24E−4	–	0.23E−4
O/H	$4.55E-4^{+4.7E-5}_{-4.2E-5}$	$3.97E-4^{+4.8E-5}_{-4.8E-5}$	5.16E−4	5.22E−4	5.29E−4	3.80E−4	$5.55E-4^{+7.9E-5}_{-6.9E-5}$	$5.24E-4^{+6.2E-5}_{-5.3E-5}$	5.59E−4	2.8E−4	4.4E−4	4.4E−4
Ne/H	$1.48E-4^{+2.2E-5}_{-1.9E-5}$	$1.47E-4^{+1.7E-5}_{-1.4E-5}$	1.76E−4	1.5E−4	1.5E−4	–	$1.45E-4^{+2.3E-5}_{-2.0E-5}$	$1.58E-4^{+2.1E-5}_{-2.1E-5}$	1.36E−4	0.86E−4	5.13E−5	–
Ar/H	$6.27E-7^{+1.1E-7}_{-9.2E-8}$	$6.27E-7^{+1.1E-7}_{-9.2E-8}$	1.43E−6	–	2.82E−6	–	$2.40E-7^{+4.6E-8}_{-3.9E-8}$	$2.40E-7^{+4.6E-8}_{-3.9E-8}$	3.06E−7	–	2.09E−6	–
S/H	$2.28E-6^{+4.7E-7}_{-3.9E-7}$	$2.50E-6^{+5.3E-7}_{-6.2E-7}$	0.16E−5	–	3.1E−6	–	$1.20E-5^{+3.1E-6}_{-2.4E-6}$	$1.01E-5^{+2.2E-6}_{-1.1E-6}$	0.71E−5	–	5.37E−6	–
Cl/H	$5.45E-8^{+7.7E-9}_{-6.8E-9}$	$5.79E-8^{+8.5E-9}_{-9.2E-9}$	0.84E−7	–	–	–	$2.83E-7^{+5.3E-8}_{-7.0E-8}$	$2.83E-7^{+5.3E-8}_{-7.0E-8}$	1.18E−7	–	–	–
N/O	0.46	0.52	0.37	–	–	–	0.12	0.26	0.10	–	–	–

References: (1) Milingo et al. (2002); (2) Kingsburgh & Barlow (1994); (3) Maciel & Quireza (1999); (4) Chiappini & Maciel (1994).

Table 6. Abundances derived from the NEAT for Hen2-29 and Hen2-37 compared with other works. Neat (1) and Neat (2) refer to the derived abundances using the ICF of Kingsburgh & Barlow (1994) and Delgado-Inglada et al. (2014), respectively.

Element	Hen2-29 Neat(1)	Neat (2)	Ref 1	Ref 2	Ref 3	Hen2-37 Neat(1)	Neat (2)	Ref 1	Ref 2	Ref 3	Ref 4	Ref 5
He/H	$1.26E-1^{+7.3E-3}_{-7.3E-3}$	$1.26E-1^{+4.9E-3}_{-4.9E-3}$	1.09E−1	1.08E−1	–	$1.17E-1^{+4.0E-3}_{-4.0E-3}$	$1.17E-1^{+4.0E-3}_{-4.0E-3}$	1.04E−1	1.19E−1	–	1.20E−1	–
C/H	$1.63E-3^{+2.2E-4}_{-2.2E-4}$	$1.63E-3^{+2.2E-4}_{-2.2E-4}$	–	–	–	$7.56E-4^{+1.2E-4}_{-1.1E-4}$	$7.56E-4^{+1.3E-4}_{-1.3E-4}$	–	–	–	–	–
N/H	$2.17E-4^{+2.5E-5}_{-3.6E-5}$	$1.80E-4^{+2.1E-5}_{-2.5E-5}$	1.39E−4	1.66E−4	–	$3.18E-4^{+5.0E-5}_{-3.8E-5}$	$2.40E-4^{+3.1E-5}_{-4.2E-5}$	2.20E−4	2.36E−4	–	3.52E−4	3.89E−4
O/H	$3.77E-4^{+3.8E-5}_{-3.1E-5}$	$3.79E-4^{+3.9E-5}_{-3.2E-5}$	4.04E−4	4.15E−4	4.17E−4	$7.08E-4^{+6.4E-5}_{-7.5E-5}$	$7.23E-4^{+6.7E-5}_{-7.1E-5}$	9.34E−4	8.42E−4	9.12E−4	11.0E−4	11.2E−4
Ne/H	$1.01E-4^{+8.4E-5}_{-8.5E-5}$	$8.67E-5^{+7.7E-6}_{-8.2E-6}$	1.09E−4	4.81E−5	5.01E−5	$1.52E-4^{+1.4E-5}_{-1.3E-5}$	$1.41E-4^{+1.2E-5}_{-1.7E-5}$	2.30E−4	2.0E−4	1.73E−4	2.48E−4	1.02E−4
Ar/H	$1.55E-6^{+2.3E-7}_{-2.3E-7}$	$1.96E-6^{+4.0E-7}_{-3.8E-7}$	1.27E−6	1.37E−6	1.38E−6	$2.10E-6^{+3.9E-7}_{-2.7E-7}$	$3.17E-6^{+6.1E-7}_{-8.6E-7}$	2.86E−6	2.91E−6	–	4.75E−6	–
S/H	$4.95E-6^{+5.5E-7}_{-6.6E-7}$	$6.31E-6^{+7.1E-7}_{-9.8E-7}$	6.44E−6	9.07E−6	9.12E−6	$8.51E-6^{+1.1E-6}_{-1.2E-6}$	$1.20E-5^{+2.2E-6}_{-1.6E-6}$	6.60E−6	6.73E−6	–	4.5E−6	1.35E−5
Cl/H	$1.14E-7^{+1.1E-8}_{-1.1E-8}$	$1.39E-7^{+1.5E-8}_{-1.7E-8}$	–	–	–	$2.08E-7^{+2.2E-8}_{-2.3E-8}$	$2.73E-7^{+2.8E-8}_{-3.3E-8}$	–	–	–	2.98E−7	–
N/O	0.54	0.48	0.34	–	–	0.40	0.33	–	–	0.24	0.32	–

References: (1) Perinotto et al. (2004); (2) Kingsburgh & Barlow (1994); (3) Maciel & Quireza (1999); (4) Milingo et al. (2002); (5) Martins & Viegas (2000).

Table 7. Radial and expansion velocities and distances of the sample.

Object	RV$_{hel}$ (km s^{-1}) Ours	literature	V_{exp} (km s^{-1}) [S II]	[N II]	Distance (kpc) (I)	(II)	Excitation class (I)	(II)
M3-4	25.0 ± 3.24	74 ± 40 (1), 35.4 ± 4.6 (3)	18.7	17.5	3.82	4.27	6.2	7.8
M3-6	31.1 ± 3.5	49.7 ± 16.6 (1)	22.2	28.3	3.05	3.05	4.6	4.6
Hen2-29	19.8 ± 2.9	25 ± 6 (2)	33.8	29.1	4.02	4.32	8.0	10.5
Hen2-37	− 12.5 ± 3.12	12 ± 5 (2)	47.9	52.2	3.35	4.01	8.4	11.4

References: (1) Schneider & Terzian (1983), (2) Meatheringham, Wood & Faulkner (1988), (3) Kniazev (2012).
Distances: scales; (I) Ali, Ismail & Alsolami (2015a); (II) Frew, Parker & Bojičić (2016).
Excitation class: (I) Meatheringham & Dopita (1991); (II) Reid & Parker (2010).

Faundez-Abans & Maciel (1987) developed the Peimbert classification scheme by dividing the Peimbert type II into type IIa and type IIb. This division was proposed based essentially on the nitrogen abundances. They show that type IIa are of nitrogen abundances (log (N/H)+12 ≥ 8.0) larger than that of type IIb (log (N/H)+12 ≤ 8.0). Following the further re-analysis of Peimbert types suggested by Quireza et al. (2007), we find that both M3-4 and Hen2-37 are consistent with being of type IIa (log(N/H) + 12 ≥ 8.0 and N/O ≥ 0.25, but He/H ≤ 0.125). Therefore, they should arise from an older and less massive main-sequence population (1.2–2.4 M$_\odot$) than the type I objects. Furthermore, the spatial and kinematic properties of M3-4 (336 pc and 29.9 km s^{-1}) and Hen2-37 (185 pc and 7.3 km s^{-1}) show that they are thin Galactic disc members. M3-6 nebula is the only PN in the set that shows (log(N/H) + 12 < 8.0). The object lies at $z = 144$ pc and has $V_P = 7.3$ km s^{-1}; hence, it can be classified as a type IIb PN.

5 KINEMATICAL PARAMETERS AND DISTANCES

In order to determine the evolutionary status of a PN, we need its expansion velocity (V_{exp}) and its distance. Here, we determined V_{exp} from the two emission lines [S II] and [N II] which lie in the red channel of WiFeS instrument with the higher spectral resolution ($R \sim 7000$). The FWHM of each line was measured using the IRAF splot task. The expansion velocity was corrected for instrumental and thermal broadening following (Gieseking, Hippelein & Weinberger 1986). The results were listed in Table 7.

Hen2-37 has the highest expansion velocity, and in this object double-peak nebular emission lines are clearly seen. For Hen2-29, we derive V_{exp} – greater than the standard value of 20 km s^{-1} (Weinberger 1989). Meatheringham et al. (1988) report expansion velocities of 23.6 and 30.7 km s^{-1} for Hen2-29 and Hen2-37, respectively. These are smaller than we determine, but this is to
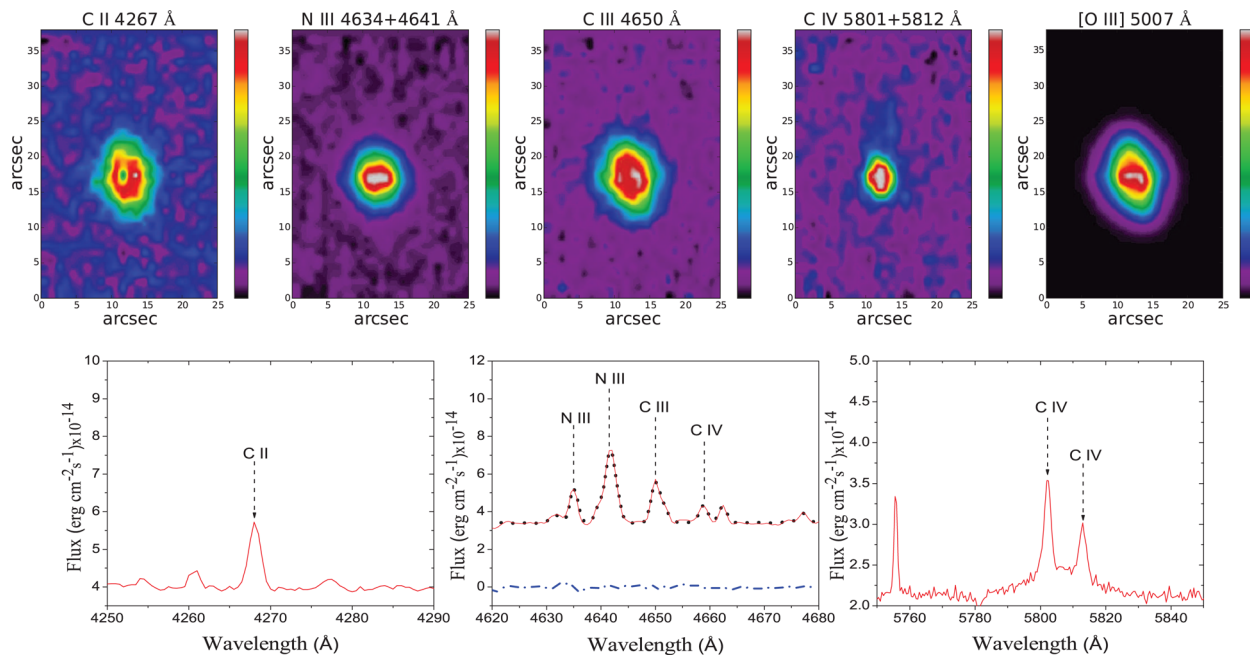
Figure 5. Emission-line maps of M3-6 nebula in the recombination lines: C II at 4267 Å; N III at 4634 Å+4641 Å; C III at 4650 Å; C IV at 5801 Å+5812 Å (sorted from left to right). All emission-line maps reveal that these recombination lines are spatially extended, and therefore they originate from the nebulae, with the exception of C IV at 5801 Å+5812 Å which is probably emitted from the central nebular star. In the upper-right panel, we present an emission-line map of M3-6 in the CEL of [O III] at 5007 Å for comparison. The lower panels show the characteristic emission lines (in red colour) from the M3-6 spectrum which are generally used to classify nebular CS as a WELS type. In the lower-middle panel, the black dotted line shows the Gaussian fit of the observed N III, C III and C IV recombination nebular lines, while the blue dash–dotted line shows the residual between the observed and fitted fluxes.

be expected since the Meatheringham et al. ([1988](#)) results rely on the [O III] emission line which has higher ionization potential than the lines we used, and is therefore produced closer to the centre of the nebula – see the central panels Figs [3](#) and [4](#).

The systemic velocities RV_{sys} of the sample were measured using the emsao task of the IRAF package. The RV_{sys} were derived from the Doppler shift of [N II] 6548, Hα 6562, [N II] 6583, He I 6678, [S II] 6716 and [S II] 6730 Å emission lines. We select these lines because they are located in the high spectral resolution part of nebular spectra ($R \sim 7000$). To derive the heliocentric radial velocity RV_{hel}, we used the IRAF task RVCorr to correct for the effect of the Earth's motion around the Sun. The results were presented in Table [7](#) and compared with the work of Schneider & Terzian ([1983](#), hereafter STPP83), Meatheringham et al. ([1988](#)) and Kniazev ([2012](#)). In general, the determined RV_{hel} of M3-4 nebula is relatively close to the recent estimation of Kniazev ([2012](#)) but it is smaller than that of STPP83. The value of STPP83 was originally taken from the low dispersion spectra of Mayall (1964, private communication) given as a private communication with Perek & Kohoutek ([1967](#)). The RV_{hel} for M3-6 differs significantly in accuracy with STPP83. The value of STPP83 was taken as a weighted average of two unpublished measurements 57 ± 11 (Minkowski 1957, private communication) and 12 ± 25 (Mayall 1964) as a private communication with Perek & Kohoutek ([1967](#)). This average value was weighted according to the error of each measurement. For the object Hen2-29, our derived RV_{hel} is consistent with that of MWF88 within the error range. For Hen2-37, we determined RV_{hel} of -12.5 ± 3.12 which differs significantly from that of Meatheringham et al. ([1988](#)). Our value was checked by measuring $RV_{hel} = -16.0 \pm 5.0$, from the blue part of the nebular spectrum (which has lower resolution, $R = 3000$, than the red). Three possible explanations can be

provided for this discrepancy. (1) The different spectrum resolution particularly most of nebular lines appear of double peaks due to the high expansion velocity of the nebula. (2) The radial velocity determined here was measured from integrated spectrum over the whole object. (3) The negative sign of the radial velocity measure given by Meatheringham et al. ([1988](#)) was simply missed.

None of the sample has a distance determined from either the trigonometric, spectroscopic, cluster membership or expansion methods. Therefore, we must rely on the statistical approaches to estimate distances, recognizing the large errors that this entails. We adopt here the average distance derived from the recent two distance scales of Ali et al. ([2015a](#)) and Frew et al. ([2016](#)), for each PN. The Ali et al. ([2015a](#)) scale depends on the mass–radius and radio surface brightness temperature–radius empirical relationships, and specifically on the nebular angular size and 5 GHz radio flux. The Frew et al. ([2016](#)) scale depends on the empirical relationship between Hα surface brightness and the radius of PN, using the nebular angular size and the Hα flux. The results of the two approaches are given in Table [6](#). Both methods give roughly the same distances. The angular radii of the PNe are taken from Frew et al. ([2016](#)), while radio fluxes at 5 GHz were taken from Cahn, Kaler & Stanghellini ([1992](#)) except for M3-4. We find that this object has radio fluxes which differ between the different references. We adopted here the average value from Milne & Aller ([1975](#)), Milne ([1979](#)), Zijlstra, Pottasch & Bignell ([1989](#)) and Cahn et al. ([1992](#)).

6 THE CS OF M3-6

Tylenda, Acker & Stenholm ([1993](#)), Marcolino & de Araújo ([2003](#)) and Weidmann & Gamen ([2011](#)) classified the CS of the M3-6 nebula as being of the WELS type. Miszalski ([2009](#)) reported that
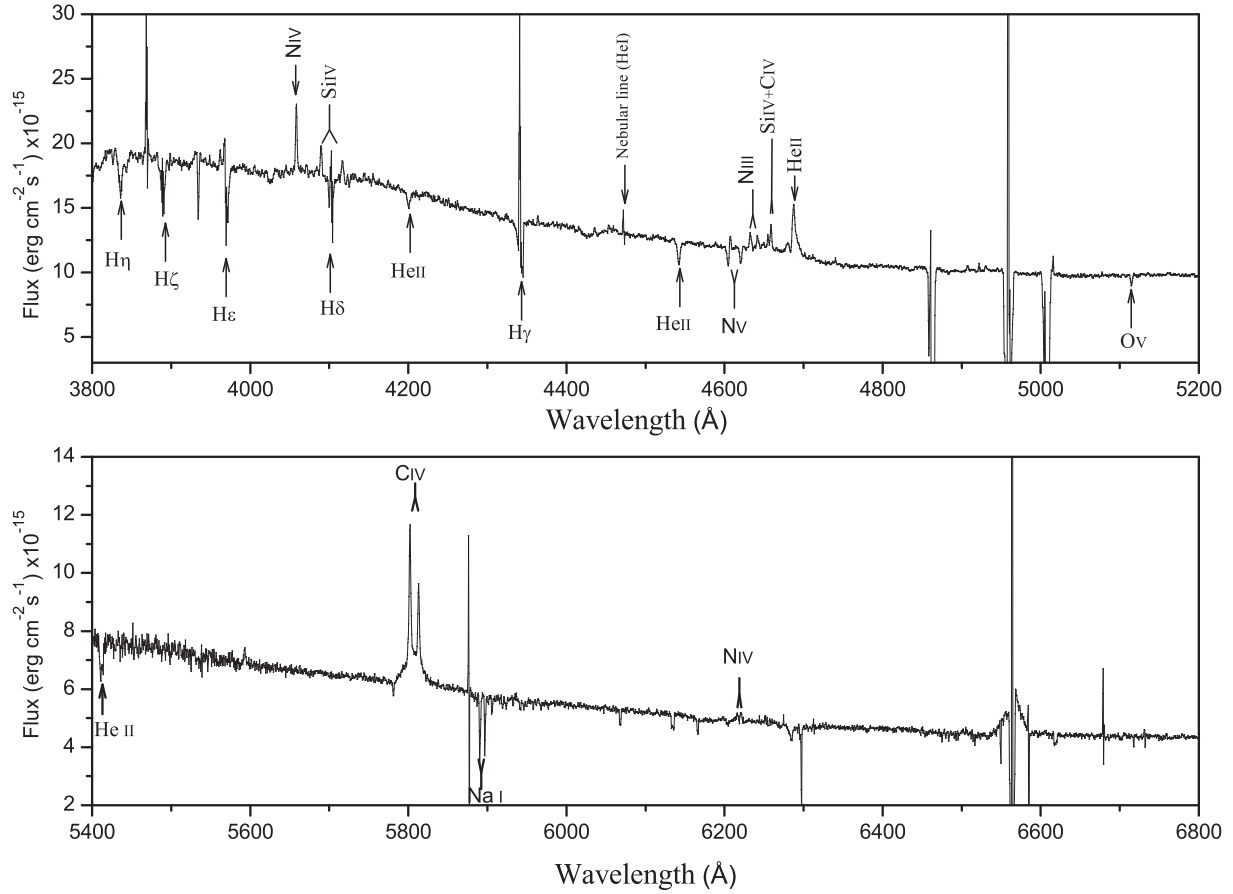
Figure 6. The nebular subtracted spectrum of the CS in M3-6. The blue spectrum (upper panel) shows clearly the presence of Balmer and He II lines in absorption, with the exception of He II λ4686 which is seen in emission. The red spectrum (lower panel) is characterized by the presence of C IV doublet lines at λλ5801, 5811, N IV at λλ6212, 6220and the interstellar Na I D lines at λλ5890, 5896seen in absorption. More discussion on this CS spectrum and the stellar classification derived from it is given in the text.

many of WELS are probably misclassified close binaries. Further, Miszalski et al. (2011) and Corradi et al. (2011) observed many of WELS emission lines in the spectra of stars known to be close binary systems, and explained that these lines were originated from the irradiated zone on the side of the companion facing the primary.

Basurah et al. (2016) claimed that, for many objects, the WELS class of the PNe CS may be spurious. From WiFeS data of NGC 5979, M4-2 and My60, they showed that the characteristic CS recombination lines of WELS type are of nebular origin. Specifically, the lines used to provide the WELS classification are C II at 4267 Å, N III at 4634, 4641 Å, C III at 4650 Å, and C IV at 5801 and 5812 Å. The CS classification and the WELS class in general were discussed in detail by Basurah et al. (2016). Here, we have found a further example that increases the doubt regarding the reliability of the WELS classification. In Fig. 5, we show emission-line maps of M3-6 in four CS emission lines, C II, C III, C IV and N III used to define the WELS class. It is apparent that the emission of these lines is spatially distributed over a large area of the nebula, and hence is clearly of nebular rather than of CS origin. Only in C IV at 5801 and 5812 Å is the emission limited to the central nebular region and consequently probably originates on the CS.

In fact, we can provide a revised classification for this CS based upon our own data. In Fig. 6, we show our complete extracted spectrum of the CS of M3-6. To obtain this, we carefully removed the nebular emission determined from a zone around the CS from the spaxels defining the continuum image of the CS in the image cube. Many Balmer and He II lines are clearly visible in absorption in the blue spectrum (upper panel), except He II at λ4686 appears in emission. Further, many other emission lines are present such as N IV λ4058, Si IV λλ4089, 4116, 4654, C IV λ4658 and N III λλ4634, 4640. The N V doublet λλ4604, 4620and the O V line at λ5114 both appear in absorption. In the red spectrum (lower panel), the C IV doublet λλ5801, 5811and the N IV doublet λλ6212, 6220 are clearly seen in emission, while He II λ5412 and the interstellar lines of Na I D λλ5890, 5896 are visible in absorption.

Following the CS classification scheme of Mendez (1991) and improvements given to this scheme by Weidmann, Méndez & Gamen (2015), we classify the CS of M3-6 nebula as an H-rich star of spectral type O3 I(f*). The relative weakness of the N V λλ4604, 4620 doublet compared to the He II λ4541 line is an indication of a spectral type O3, and the presence of the N III λλ4634, 4640 doublet along with the He II λ4686 line is a feature of Of(H) type. Further, the stronger emission of N IV λ4058 relative to N III λ4640 provides the * qualifier which is a unique property of stars of the O3 type (Walborn & Howarth 2000). In general, the Si IV emission is also present in Of* spectra. From Fig. 6, it appears that the C IV recombination lines at λλ5801, 5811are of CS origin – as is also revealed in the emission-line map of the nebula constructed in these two lines and shown in Fig. 5.

7 CONCLUSIONS

In this paper, we presented the first integral field spectroscopy of the southern PNe M3-4, M3-6, Hen2-29 and Hen2-37 in the optical range 3400–7000 Å. We demonstrated the utility of these observations in both providing narrow-band data to probe the morphological and excitation structure of the nebulae and in deriving their dynamical nature, their optical thickness and their chemical enrichment characteristics.

The four PNe have different optical thickness, where M3-6 is optically thin, Hen2-37 is optically thick while M3-4 and Hen2-29 are partially optically thick. From the strength of He II line, we derived EC 6.2-7.8, 4.6, 8.0-10.5 and 8.4-11.4 for M3-4, M3-6, Hen2-29 and Hen2-37, respectively. From the chemical analysis of the sample based upon integral spectroscopy, we provided Peimbert types I, IIa, IIa, IIb for Hen2-29, M3-4, Hen2-37 and M3-6, respectively, and noted that the long-slit spectroscopic data can provide surprisingly good results even though only a sub-region of the PN is analysed by this technique.

In the case of M3-6, we find that the majority of the recombination lines used in the literature to classify the CS as a WELS are in fact of nebular origin. Instead, we classify the CS as H-rich and of spectral type O3 I(f*). This result extends to five [M3-6 and NGC 3211, NGC 5979, My 60, M4-2 that are mentioned in Basurah et al. (2016)], the number of cases of misclassification of WELS stars discovered using integral field spectroscopy and served to increase doubts regarding the reliability of the WELS classification in general. In this, we support the conclusions of Weidmann et al. (2015) who observed 19 objects with the WELS classification amongst the total of 72 so classified. They concluded that 'the denomination WELS should not be taken as a spectral type, because, as a WELS is based on low-resolution spectra, it cannot provide enough information about the photospheric H abundance'.

ACKNOWLEDGEMENTS

REFERENCES

Acker A., Raytchev B., Stenholm B., Tylenda R., 1991, A&AS, 90, 89
Akras S., Gonçalves D. R., 2016, MNRAS, 455, 930
Akras S., Clyne N., Boumis P., Monteiro H., Gonçalves D. R., Redman M. P., Williams S., 2016, MNRAS, 457, 3409
Ali A., Ismail H. A., Alsolami Z., 2015a, Ap&SS, 357, 21
Ali A., Amer M. A., Dopita M. A., Vogt F. P. A., Basurah H. M., 2015b, A&A, 583, A83
Aller A., Miranda L. F., Olguín L., Vázquez R., Guillén P. F., Oreiro R., Ulla A., Solano E., 2015, MNRAS, 446, 317
Balick B., Preston H. L., Icke V., 1987, AJ, 94, 1641
Balick B., Rugers M., Terzian Y., Chengalur J. N., 1993, ApJ, 411, 778
Balick B., Perinotto M., Maccioni A., Terzian Y., Hajian A., 1994, ApJ, 424, 800
Basurah H. M., Ali A., Dopita M. A., Alsulami R., Amer M. A., Alruhaili A., 2016, MNRAS, 458, 2694
Cahn J. H., Kaler J. B., Stanghellini L., 1992, A&AS, 94, 399
Chiappini C., Maciel W. J., 1994, A&A, 288, 921
Childress M. J., Vogt F. P. A., Nielsen J., Sharp R. G., 2014, Ap&SS, 349, 617
Corradi R. L. M., Aznar R., Mampaso A., 1998, MNRAS, 297, 617
Corradi R. L. M. et al., 2011, MNRAS, 410, 1349
Danehkar A., 2015, ApJ, 815, 35
Danehkar A., Parker Q. A., 2015, MNRAS, 449, L56

De Freitas Pacheco J. A., Maciel W. J., Costa R. D. D., 1992, A&A, 261, 579
Delgado-Inglada G., Morisset C., Stasińska G., 2014, Rev. Mex. Astron. Astrofis. Ser. Conf., 44, 17
Dopita M. A., 1997, ApJ, 485, L41
Dopita M., Hart J., McGregor P., Oates P., Bloxham G., Jones D., 2007, Ap&SS, 310, 255
Dopita M. et al., 2010, Ap&SS, 327, 245
Faundez-Abans M., Maciel W. J., 1987, A&A, 183, 324
Frew D. J., Bojičić I. S., Parker Q. A., 2013, MNRAS, 431, 2
Frew D. J., Parker Q. A., Bojičić I. S., 2016, MNRAS, 455, 1459
García-Rojas J., Corradi R. L. M., Monteiro H., Jones D., Rodríguez-Gil P., Cabrera-Lavers A., 2016, ApJ, 824, L27
Gieseking F., Hippelein H., Weinberger R., 1986, A&A, 156, 101
Gilmore G., Reid N., 1983, MNRAS, 202, 1025
Girard P., Köppen J., Acker A., 2007, A&A, 463, 265
Górny S. K., Schwarz H. E., Corradi R. L. M., Van Winckel H., 1999, A&AS, 136, 145
Guerrero M. A., Toalá J. A., Medina J. J., Luridiana V., Miranda L. F., Riera A., Velázquez P. F., 2013, A&A, 557, A121
Hajian A. R. et al., 2007, ApJS, 169, 289
Howarth I. D., 1983, MNRAS, 203, 301
Kaler J. B., Jacoby G. H., 1989, ApJ, 345, 871
Kingsburgh R. L., Barlow M. J., 1994, MNRAS, 271, 257
Kniazev A. Y., 2012, Astron. Lett., 38, 707
Liu X.-W., Storey P. J., Barlow M. J., Clegg R. E. S., 1995, MNRAS, 272, 369
Maciel W. J., Dutra C. M., 1992, A&A, 262, 271
Maciel W. J., Quireza C., 1999, A&A, 345, 629
Manchado A., Guerrero M. A., Stanghellini L., Serra-Ricart M., 1996, The IAC Morphological Catalog of Northern Galactic Planetary Nebulae. Instituto de Astrofisica de Canarias, La Laguna, Spain (Foreword by Stuart R. Pottasch)
Marcolino W. L. F., de Araújo F. X., 2003, AJ, 126, 887
Martins L. P., Viegas S. M. M., 2000, A&A, 361, 1121
Meatheringham S. J., Dopita M. A., 1991, ApJS, 75, 407
Meatheringham S. J., Wood P. R., Faulkner D. J., 1988, ApJ, 334, 862
Mendez R. H., 1991, in Crivellari L., Hubeny I., Hummer D. G., eds, Proc. Advanced Research Workshop, Stellar Atmospheres: Beyond Classical Models. D. Reidel Publishing Co., Dordrecht, Trieste, p. 331
Mendoza C., 1983, in Flower D. R., ed., Proc. IAU Symp. 103, Planetary Nebulae. Reidel, Dordrecht, p. 143
Milingo J. B., Henry R. B. C., Kwitter K. B., 2002, ApJS, 138, 285
Milne D. K., 1979, A&AS, 36, 227
Milne D. K., Aller L. H., 1975, A&A, 38, 183
Miranda L. F., Ramos-Larios G., Guerrero M. A., 2010, PASA, 27, 180
Miszalski B., 2009, PhD thesis, Department of Physics, Macquarie University, Sydney, Australia
Miszalski B., Corradi R. L. M., Boffin H. M. J., Jones D., Sabin L., Santander-García M., Rodríguez-Gil P., Rubio-Díez M. M., 2011, MNRAS, 413, 1264
Monreal-Ibero A., Roth M. M., Schönberner D., Steffen M., Böhm P., 2005, ApJ, 628, L139
Peimbert M., Torres-Peimbert S., 1983, in Flower D. R., ed., Proc. IAU Symp. 103, Planetary Nebulae. Reidel, Dordrecht, p. 233
Perinotto M., Morbidelli L., Scatarzi A., 2004, MNRAS, 349, 793
Perek L., Kohoutek L., 1967, Catalog of Galactic Planetary Nebulae Czechoslovakian Academy of Sciences, Prague
Quireza C., Rocha-Pinto H. J., Maciel W. J., 2007, A&A, 475, 217
Reid W. A., Parker Q. A., 2010, PASA, 27, 187
Schneider S. E., Terzian Y., 1983, ApJ, 274, L61 (STPP83)
Steffen W., López J. A., Lim A. J., 2002, Rev. Mex. Astron. Astrofis. Ser. Conf., 13, 150
Storey P. J., Zeippen C. J., 2000, MNRAS, 312, 813
Tsamis Y. G., Walsh J. R., Pequignot D., Barlow M. J., Liu X.-W., Danziger I. J., 2007, The Messenger, 127, 53
Tylenda R., Acker A., Stenholm B., Koeppen J., 1992, A&AS, 95, 337

Tylenda R., Acker A., Stenholm B., 1993, A&AS, 102, 595
Vázquez R., 2012, ApJ, 751, 116
Walborn N. R., Howarth I. D., 2000, PASP, 112, 1446
Weidmann W. A., Gamen R., 2011, A&A, 526, A6
Weidmann W. A., Méndez R. H., Gamen R., 2015, A&A, 579, A86
Weinberger R., 1989, A&AS, 78, 301
Wesson R., Stock D. J., Scicluna P., 2012, MNRAS, 422, 3516
Zijlstra A. A., Pottasch S. R., Bignell C., 1989, A&AS, 79, 329

SUPPORTING INFORMATION

Additional Supporting Information may be found in the online version of this article:

Table 2. Integrated line fluxes and the derived de-reddened line intensities for M3-4, M3-6, Hen2-29 and Hen2-29. Absolute line fluxes for Hβ are given in the text. The C IV doublet lines 5801+5812 Å are of CS origin.
(http://www.mnras.oxfordjournals.org/lookup/suppl/doi:10.1093/mnras/stw1744/-/DC1).

Please note: Oxford University Press is not responsible for the content or functionality of any supporting materials supplied by the authors. Any queries (other than missing material) should be directed to the corresponding author for the article.

This paper has been typeset from a TeX/LaTeX file prepared by the author.